

# Exciton-polariton condensates in van der Waals magnetic microwires

Heng Zhang<sup>1,†</sup>, Niloufar Nilforoushan<sup>1,6,†</sup>, Christian Weidgans<sup>1</sup>, Julian Hirschmann<sup>4,5</sup>, Imke Gronwald<sup>1</sup>,  
Kseniia Mosina<sup>2</sup>, Zdeněk Sofer<sup>2</sup>, Fabian Mooshammer<sup>3</sup>, Florian Dirnberger<sup>4,5,\*</sup>, and Rupert Huber<sup>1,3</sup>

<sup>1</sup>*Department of Physics, University of Regensburg, 93040 Regensburg, Germany*

<sup>2</sup>*Department of Inorganic Chemistry, University of Chemistry and Technology Prague,  
166 28 Prague 6, Czech Republic*

<sup>3</sup>*Regensburg Center for Ultrafast Nanoscopy, University of Regensburg, 93040 Regensburg, Germany*

<sup>4</sup>*Zentrum für QuantumEngineering (ZQE), Technical University of Munich, Garching, Germany*

<sup>5</sup>*Department of Physics, Technical University of Munich, Munich, Germany*

<sup>6</sup>*present address: Université Paris Cité, CNRS, LMPQ, Paris, France*

<sup>†</sup>*These authors contributed equally*

*\*corresponding author: f.dirnberger@tum.de*

**Quasiparticle condensates are among the most spectacular solid-state manifestations of quantum physics. Coupling macroscopic real-space wave functions to other degrees of freedom, such as the electron spin, could add valuable control knobs for quantum applications. While creating spin-carrying superconducting condensates has attracted enormous attention, man-made condensates of light-matter hybrids known as exciton-polaritons have lacked a comparable spin-related perspective. Here we open a new door by demonstrating exciton-polariton condensation in the antiferromagnetic semiconductor CrSBr, a van der Waals material with strongly intertwined optical and magnetic properties. Under photoexcitation, CrSBr microwires embedded in an optical cavity show the hallmarks of polariton condensation: a dramatic increase of the emission intensity from an excited laterally confined polariton state by multiple orders of magnitude, spectral narrowing of the emission line, and an intriguing continuous shift of the peak energy. Interferometry evidences an increase of spatial and temporal coherence. The conditions for efficient optical pumping suggest a crucial role of surface excitons and ultrafast polariton-magnon scattering. Our results highlight CrSBr microwires as a promising platform for exploring magnetically tunable polariton condensates, their directional propagation and their potential for spin-based quantum devices.**

## Introduction

Non-equilibrium Bose-Einstein condensates in condensed-matter systems have attracted a growing interest as a platform for realizing and exploring macroscopic quantum phenomena<sup>1,2</sup>. They represent a highly coherent many-body quantum state that can exhibit superfluid propagation<sup>3</sup> and pronounced nonlinear interactions<sup>4</sup>. Among them, condensates of hybrid light-matter quasiparticles<sup>5,6</sup>, so-called exciton-polaritons, are particularly promising owing to the unique combination of photonic coherence and excitonic interactions, which makes them a potential platform for applications in quantum communication and cryptography<sup>7,8</sup>. The key challenge, however, lies in controlling the coherent condensate emission. So far, most polariton condensates have been realized in conventional semiconductor microcavities where quasiparticle interactions are weak and tunability typically requires a modification of the structure. Quantum materials that mediate efficient interactions of exciton-polaritons with other quasiparticles, such as phonons or magnons, could provide a compelling path forward. While proximitizing superconducting condensates with spin-ordered materials has led to new functionalities<sup>9-12</sup>, exciton-polariton condensation in spin-ordered systems remains largely unexplored.

Magnetic van der Waals (vdW) crystals<sup>13-15</sup> have recently emerged as a highly attractive class of quantum materials that support profound interactions between excitons, photons, phonons, and magnons<sup>16-21</sup>. Particularly the air-stable layered A-type antiferromagnet CrSBr stands out for its tightly bound, quasi-one-dimensional excitons which are polarized along the crystallographic *b*-axis with giant oscillator strength<sup>22</sup>. A schematic of its crystal structure is shown in Fig. 1a. The most prominent exciton resonance of bulk CrSBr occurs near an energy of 1.36 eV. At the surface, however, this resonance is shifted. In few-layer crystals on standard dielectric substrates, it appears at 1.34 eV (ref. <sup>23</sup>). Thus far, studies have explored the strong coupling of excitons to vertically confined photon modes in bulk crystals. In these multimode optical cavities, new magneto-optic correlations<sup>24,25</sup>, hyperbolic effects<sup>26</sup>, extreme anisotropy<sup>27</sup>, and most recently, signatures of bulk polariton condensation<sup>28</sup> have been found to emerge. In addition to the vertical direction, exfoliated flakes of CrSBr may also confine photons laterally. Due to weaker atomic bonds in the

*b*-axis, CrSBr naturally forms microscopic wires which are strongly elongated in the *a*-axis, effectively realizing a slab waveguide geometry which is ideal for exploring enhanced photon confinement.

Here, we demonstrate the condensation of exciton-polaritons in such CrSBr microwires. Under near-resonant ultrafast optical excitation, our microwires show the fingerprint of polariton condensation – that is, a dramatic increase in the photoluminescence (PL) intensity accompanied by linewidth narrowing and a pronounced energy shift. Above the excitation threshold, optical interferometry of the PL emission reveals a clear increase in its spatial and temporal coherence. Efficient optical pumping substantially below the bulk exciton resonance suggests a crucial role of surface excitons and ultrafast polariton-magnon scattering. The exciton-polariton condensates in CrSBr shown by our study open new avenues for designing and controlling waveguide-coupled coherent emission by external magnetic fields, magnons, and spin fluctuations, highlighting new directions for photonic quantum technologies.

### **Magnetic microwire polaritons**

To achieve strong coupling between bulk excitons and a single photon mode confined in the vertical direction, CrSBr crystals with a thickness of a few nanometres are centred between two planar cavity mirrors. First, a 200-nm-thick gold mirror is evaporated on a silicon wafer and covered by a spacer layer of PMMA with a nominal thickness of 70 nm. Subsequently, CrSBr crystals are transferred onto the substrate by mechanical exfoliation, capped by another 70 nm PMMA spacer layer and a semi-transparent, 40-nm-thin gold mirror to complete the microcavity structure. In an optical microscope, we identify few-layer CrSBr crystals that are elongated along the crystallographic *a*-axis with typical lengths of tens of  $\mu\text{m}$ , but exhibit a small width of approximately 1  $\mu\text{m}$  in the *b*-direction. Figure 1b displays the optical micrograph of an exemplary microcavity.

Such structures can act as microwires that spatially confine light similar to slab waveguides. The most rigorous confinement is given by the two narrowly spaced microcavity mirrors in the vertical (*c*-axis) direction. The resulting strong coupling with the bulk exciton resonance and the emergent polaritonic effects are thus overall well-described by numerical calculations assuming infinite lateral crystal extensions

(see Extended Data Fig. 1). A narrow lateral width of the flake along the  $b$ -axis, however, causes additional quantization effects (Fig. 1b, inset), which are less relevant along the  $a$ -axis owing to the extended wire length in this direction. This situation can be qualitatively captured by modelling the polariton as a particle in an elongated 2D rectangular potential well (see Methods). The model predicts that the confinement causes a sequence of discrete quantized polariton states along the  $b$ -axis with energy splittings on the order of tens of meV (Fig. 1c). Since the polaritons are barely restricted along the  $a$ -axis, the dispersion of the various polariton branches remains essentially parabolic along this direction (Fig. 1d).

We measured the polariton PL emission of our microwires in the antiferromagnetic phase (lattice temperature,  $T_L = 5$  K) where the spins are aligned antiparallel between adjacent layers (Fig. 1a). Orienting CrSBr wires parallel or perpendicular to the entrance slit of the spectrometer allows us to image the polaritonic band dispersion along the two orthogonal angles  $\theta_a$  and  $\theta_b$  (Fig. 1c,d, insets). Light emitted at an angle  $\theta_{a,b}$  originates from exciton-polaritons with energy  $E$  and in-plane momentum  $k_{a,b}$  following  $k_{a,b} = (E/\hbar c)\sin\theta_{a,b}$ .<sup>1,5,29</sup> As an example, we discuss the polariton emission of a CrSBr cavity with a width of  $W \approx 1.25$   $\mu\text{m}$ , and a length of  $L \approx 40$   $\mu\text{m}$  that we labelled cavity #1 (Extended Data Fig. 1a), which was measured using optical pump pulses with a pulse duration of 140 fs centred at a photon energy of  $\hbar\omega_{\text{pump}} = 1.771$  eV (repetition rate, 85 kHz).

Resolving the PL spectra along the  $b$ -axis for a range of emission angles  $-25^\circ < \theta_b < 25^\circ$ , we observe discrete features consistent with the lateral quantization of polaritons in narrow optical waveguides (Fig. 1e). To enhance the visibility of the higher lying, weakly emissive excited states, we multiply the PL intensity in this region (marked by a white box) by a factor of 2. Thus, several quantized modes can be clearly recognized, including the ground state ( $Q_0$ ), the first excited state ( $Q_1$ ) and the second excited state ( $Q_2$ ) at energies of 1.248 eV, 1.265 eV and 1.286 eV, respectively. Conversely, the measured PL emission of this wire along the  $a$ -direction displays a series of dispersive, parabolic polariton modes exhibiting minima at those energies (Fig. 1f). This is in line with the negligible quantization expected for the extended dimension of our cavity along the  $a$ -axis. Details of the dispersion vary between samples owing to

differences in the thickness and the width of the wires, yet they all exhibit features indicative of polariton confinement in microwires (Extended Data Figs. 3 and 5)<sup>30-32</sup>, that is a continuous parabolic dispersion along the long axis ( $a$ -axis) and discrete energy states along the short axis ( $b$ -axis), consistent with the simulation predictions in Fig. 1c,d.

For a quantitative analysis of the exciton-photon coupling strength in our magnetic microwires, we implemented a global fit to the quantized and parabolically dispersed polariton states by a coupled oscillator model (Fig. 1e,f, coloured dots and white lines; see Methods for details). The good agreement with the experimental data indicates that these modes correspond to the lower polariton emission of a 9 nm-thick (about 10 layers) CrSBr crystal<sup>33</sup>. The fit also confirms that the interaction between vertically confined photons and excitons reaches the strong-coupling regime with a vacuum Rabi splitting of  $2\hbar\Omega_R = 200$  meV (i.e., an exciton-photon coupling strength of  $g = 100$  meV), which matches recent observations of polaritonic effects in CrSBr<sup>24,25</sup>.

Beside the PL emission of lower polaritons, we observe two isolated resonances at  $\hbar\omega \approx 1.312$  eV and 1.325 eV, which are clearly resolved along the  $a$ -axis, but also seem to overlap with discrete states quantized along the  $b$ -axis. Even though they are coupled to the same cavity mode, the absence of notable dispersion in the wave vector range measured by our experiment indicates that these two resonances remain in the weak coupling regime. Considering the different dielectric environment and strain in our cavity, these features can tentatively be ascribed to the recently identified surface excitons of CrSBr<sup>23</sup>. Independent of their origin, the existence of states at energies well below the bulk exciton resonance opens a pathway for near-resonant optical excitation of polaritons. This can favour polariton condensation, as we show below.

### **Fluence-dependent nonlinear emission**

In a polariton condensate, final-state stimulation leads to a macroscopic population of a single quantum state, which is expected to manifest in a dramatic increase of PL with increasing polariton density<sup>5,31,34</sup>. To test this scenario, we measure the PL emission of cavity #1 as a function of pump fluence  $\Phi$ . In the first experiment, we tune our pump laser into resonance with the dispersionless band at  $\hbar\omega_{\text{pump}} = 1.325$  eV.

The resulting PL spectra (Fig. 2a) unveil a strongly nonlinear fluence dependence of the intensity of the PL peak located at a photon energy of 1.276 eV. The spectrally integrated peak emission exhibits a prototypical threshold-like scaling with the pump fluence (cf. Fig. 2b). Once the fluence exceeds  $\Phi_{\text{th}} \approx 30 \mu\text{J}/\text{cm}^2$ , a moderate increase of the fluence by a mere factor of 3 causes a dramatic enhancement of the PL peak centred at  $\hbar\omega = 1.276$  eV by more than two orders of magnitude. In sharp contrast, the polariton emission scales linearly when we excite our cavities off-resonantly at  $\hbar\omega_{\text{pump}} = 1.771$  eV (Fig. 2b and Extended Data Fig. 2).

To identify which polaritonic state gives rise to such a strongly nonlinear increase of the PL emission, we acquired angle-resolved PL maps (Fig. 2c,d and Extended Data Fig. 4). The PL peak that dominates the spectrum in Fig. 2a originates from  $Q_1$  confined by our microwire in the lateral  $b$ -direction, which is separated from the pump photon energy by 49 meV. Whereas the overall PL emission of  $Q_0$  and  $Q_1$  is comparable below threshold,  $Q_1$  completely dominates the PL signal for  $\Phi > \Phi_{\text{th}}$  (Fig. 2d). The abrupt increase of the PL intensity from  $Q_1$  is accompanied by a significant decrease of its linewidth, from 19 meV to 8.7 meV, and an energy increase by almost 5 meV (cf. Fig. 2e,f). These features are unambiguous hallmarks of exciton-polariton condensation in microcavities.

### **Emergence of coherence**

Final-state stimulation, which macroscopically populates a single quantum state, inherently also synchronizes the phase of all particles contributing to the condensate. This process is expected to manifest in a spontaneous macroscopic spatial and temporal coherence. To prove this key aspect of condensation in our experiment, we finally evidence the build-up of coherence by measuring the first-order correlation function of the polariton PL emission of cavity #1 in a Michelson interferometer setup<sup>5,31</sup>. The PL emission is first split evenly into the two arms of the interferometer, and then one of the beams is inverted in a centrosymmetric way by a retroreflector. The two beams are then combined at the output of the interferometer by a lens and overlapped in the real-space image plane. Temporal overlap is achieved by delaying one arm relative to the other via an optical delay line. Figure 3a,b show the spatially overlapped

PL images at a delay time of  $\tau = 0$  fs below and above the condensation threshold, respectively. While signatures of coherence are absent below  $\Phi_{\text{th}}$ , clear interference fringes evidencing spatially coherent emission are observed as the fluence exceeds the condensation threshold.

Sweeping the delay time between the two interferometric images allows us to measure the temporal coherence of the condensate emission, as exemplarily shown in Fig. 3c. We quantify the coherence time by extracting the visibility of the interference fringes, defined as  $v = (I_{\text{max}} - I_{\text{min}})/(I_{\text{max}} + I_{\text{min}})$ , as a function of delay time  $\tau$  (see Fig. 3d-e). Here  $I_{\text{max}}$  ( $I_{\text{min}}$ ) represents the intensity of a local maximum (neighbouring minimum) of the fringes. The data are well described by a Gaussian profile with a coherence time of  $408 \pm 22$  fs, defined as the full width at half maximum (FWHM), which is significantly longer than the coherence time of the pump pulse (at  $\hbar\omega_{\text{pump}} = 1.325$  eV) of  $225 \pm 18$  fs. Thus, our experimental observations unambiguously prove that exciton-polaritons in CrSBr can undergo condensation.

## Discussion

Several unique aspects about our polariton condensates deserve particular emphasis. First, we note that in our study, condensates are only observed under near-resonant excitation (see Fig. 2b and Extended Data Fig. 2). This involves optical absorption below the main exciton resonance which can tentatively be ascribed to the existence of surface excitons in CrSBr. Paired with a large Rabi splitting that allows for efficient spectral filtering of notably different pump and emission photon energies, it makes near-resonant pumping a highly attractive experimental route to condensation. The results stand in stark contrast to those we obtain when pumping at 1.771 eV. Even though much larger polariton densities can be created at this energy owing to the strong absorption of B-excitons<sup>21,23</sup>, it seems the benefits are overshadowed by substantial lattice heating effects. Near-resonant excitation in turn significantly reduces the excess energy per absorbed photon, which ensures the lattice temperature remains low. Furthermore, the kHz repetition rate of our pulsed laser provides extended time periods between pulses during which smaller amounts of excess heat can be dissipated. These aspects are critical for achieving polariton condensation in our experiment.

Second, the fluence dependence of polariton energies observed in our study is qualitatively different from that reported previously. Thus far, either a decrease of polariton energies<sup>24,35</sup>, or a competition between opposite shifts of polariton energies<sup>28</sup> was noted in response to increasing excitation fluence. In our case, a monotonic increase of polariton energies is observed (see Fig. 2f). Creating minimal heating, it thus seems near-resonant, kHz excitation isolates a contribution to the polariton energy that shifts its states towards higher energies. This is indeed a common observation for polariton systems and typically ascribed to repulsive Coulomb interactions between excitons<sup>1,7,28,35,36</sup> or saturable absorption effects<sup>37,38</sup>. In CrSBr, however, a new effect may be taken into consideration: Ab initio calculations together with reflectance measurements recently showed that magnon-induced magnetic disorder can sizably reduce the oscillator strength of excitons in CrSBr<sup>23,26</sup>. It is therefore important to note that when excitons are strongly coupled to photons, a decrease of the oscillator strength quenches the Rabi gap which increases the lower polariton energy. This effect is particularly pronounced for lower polaritons with sizable photon fraction, like those studied in our microwires. Hence, we suggest the energy shifts shown in Fig. 2f may involve contributions, not only from exciton-exciton repulsion, but also from the (unavoidable) photoexcitation of magnons<sup>39,40</sup> and the resulting renormalization of the Rabi gap.

At last, we address the fact that polariton condensates are formed in excited states and not in the ground state of our microwires. In two of our samples (cf. Figs. 2 and Extended Data Fig. 5), the energy difference between pump photons and the excited-state condensate emission is indeed as large as the energy of an optical magnon mode of CrSBr ( $\sim 45$  meV) that was recently evidenced in neutron scattering<sup>41</sup> and terahertz absorption measurements<sup>42</sup>. We suggest that optical magnon emission could provide an ultrafast pathway for the formation of a non-equilibrium condensate in excited microwire states. At the same time, the emission of such magnons could reduce the exciton oscillator strength, potentially accounting for the observed shift of the condensate state towards higher energies.

## **Conclusion**

We demonstrate polariton condensation in microwires of the van der Waals antiferromagnet CrSBr. The polaritons are laterally quantized by the finite dimension of the microwire along its short axis. By pumping in resonance with surface exciton states of CrSBr, hallmarks of polariton condensation are observed from excited quantized states, including a multi-order increase of polariton PL emission, linewidth narrowing, energy shift and a build-up of spatial and temporal coherence. Photoexcitation with kHz repetition rate potentially isolates an intriguing property of the polariton condensate in CrSBr microcavity wires, arising from polariton-magnon interactions. Our results open exciting possibilities for interfacing the macroscopic quantum mechanical wavefunction of tailor-made condensates with spin order, magnetic control, and spintronic concepts for next-generation quantum technologies. Particularly appealing are the prospects of modulating coherent condensate emission on ultrafast timescales by coupling them to coherent, high-frequency magnons, connecting light-based communication with magnetic data storage and processing.

## References

1. Deng, H. *et al.* Exciton-polariton Bose-Einstein condensation. *Rev. Mod. Phys.* **82**, 1489-1537 (2010).
2. Bloch, J. *et al.* Non-equilibrium Bose-Einstein condensation in photonic systems. *Nat. Rev. Phys.* **4**, 470-488 (2022).
3. Amo, A. *et al.* Superfluidity of polaritons in semiconductor microcavities. *Nat. Phys.* **5**, 805-810 (2009).
4. Sanvitto, D. *et al.* All-optical control of the quantum flow of a polariton condensate. *Nat. Photonics* **5**, 610-614 (2011).
5. Kasprzak, J. *et al.* Bose-Einstein condensation of exciton polaritons. *Nature* **443**, 409-414 (2006).
6. Kéna-Cohen, S. & Forrest, S. R. Room-temperature polariton lasing in an organic single-crystal microcavity. *Nat. Photonics* **4**, 371-375 (2010).
7. Deiteil, A. *et al.* Towards polariton blockade of confined exciton-polaritons. *Nat. Mater.* **18**, 219-222 (2019).
8. Ghosh, S. & Liew, T. C. H. Quantum computing with exciton-polariton condensates. *NPJ Quantum Inf.* **6**, 16 (2020).
9. Baumgartner, C. *et al.* Supercurrent rectification and magnetochiral effects in symmetric Josephson junctions. *Nat. Nanotechnol.* **17**, 39-44 (2022).
10. Zhou, H. *et al.* Isospin magnetism and spin-polarized superconductivity in bernal bilayer graphene. *Science* **375**, 774-778 (2022).

11. Cao, Y. *et al.* Pauli-limit violation and re-entrant superconductivity in moire graphene. Nature **595**, 526-531 (2021).
12. Hu, G. *et al.* Long-range skin Josephson supercurrent across a van der Waals ferromagnet. Nat. Commun. **14**, 1779 (2023).
13. Gong, C. *et al.* Discovery of intrinsic ferromagnetism in two-dimensional van der Waals crystals. Nature **546**, 265-269 (2017).
14. Burch, K. S. *et al.* Magnetism in two-dimensional van der Waals materials. Nature **563**, 47-52 (2018).
15. Gibertini, M. *et al.* Magnetic 2D materials and heterostructures. Nat. Nanotechnol. **14**, 408-419 (2019).
16. Kang, S. *et al.* Coherent many-body exciton in van der Waals antiferromagnet NiPS<sub>3</sub>. Nature **583**, 785-789 (2020).
17. Huang, B. *et al.* Electrical control of 2D magnetism in bilayer CrI<sub>3</sub>. Nat. Nanotechnol. **13**, 544-548 (2018).
18. Vaclavkova, D. *et al.* Magnon polarons in the van der Waals antiferromagnet FePS<sub>3</sub>. Phys. Rev. B **104**, 134437 (2021).
19. Seyler, K. L. *et al.* Ligand-field helical luminescence in a 2D ferromagnetic insulator. Nat. Phys. **14**, 277-281 (2017).
20. Dirnberger, F. *et al.* Spin-correlated exciton-polaritons in a van der Waals magnet. Nat. Nanotechnol. **17**, 1060-1064 (2022).
21. Wilson, N. P. *et al.* Interlayer electronic coupling on demand in a 2D magnetic semiconductor. Nat. Mater. **20**, 1657-1662 (2021).

22. Liebich, M. *et al.* Controlling coulomb correlations and fine structure of quasi-one-dimensional excitons by magnetic order. *Nat. Mater.* **24**, 384-390 (2025).
23. Shao, Y. *et al.* Magnetically confined surface and bulk excitons in a layered antiferromagnet. *Nat. Mater.* **24**, 391-398 (2025).
24. Dirnberger, F. *et al.* Magneto-optics in a van der Waals magnet tuned by self-hybridized polaritons. *Nature* **620**, 533-537 (2023).
25. Wang, T. *et al.* Magnetically-dressed CrSBr exciton-polaritons in ultrastrong coupling regime. *Nat. Commun.* **14**, 5966 (2023).
26. Ruta, F. L. *et al.* Hyperbolic exciton polaritons in a van der Waals magnet. *Nat. Commun.* **15**, 8261 (2024).
27. Li, Q. *et al.* Two-dimensional magnetic exciton polariton with strongly coupled atomic and photonic anisotropies. *Phys. Rev. Lett.* **133**, 266901 (2024).
28. Han, B. *et al.* Exciton-polariton condensate in the van der Waals magnet CrSBr. *arXiv preprint arXiv:2501.18233* (2025).
29. Wertz, E. *et al.* Spontaneous formation and optical manipulation of extended polariton condensates. *Nat. Phys.* **6**, 860-864 (2010).
30. Su, R. *et al.* Room temperature long-range coherent exciton polariton condensate flow in lead halide perovskites. *Sci. Adv.* **4**, eaau0244 (2018).
31. Anton-Solanas, C. *et al.* Bosonic condensation of exciton-polaritons in an atomically thin crystal. *Nat. Mater.* **20**, 1233-1239 (2021).
32. Fischer, J. *et al.* Spatial coherence properties of one dimensional exciton-polariton condensates. *Phys. Rev. Lett.* **113**, 203902 (2014).

33. Lee, K. *et al.* Magnetic order and symmetry in the 2D semiconductor CrSBr. *Nano Lett.* **21**, 3511-3517 (2021).
34. Su, R. *et al.* Observation of exciton polariton condensation in a perovskite lattice at room temperature. *Nat. Phys.* **16**, 301-306 (2020).
35. Datta, B. *et al.* Magnon-mediated exciton-exciton interaction in a van der Waals antiferromagnet. *Nat. Mater.* (2025).
36. Dirnberger, F. *et al.* Spin-correlated exciton-polaritons in a van der Waals magnet. *Nat. Nanotechnol.* **17**, 1060-1064 (2022).
37. Yagafarov, T. *et al.* Mechanisms of blueshifts in organic polariton condensates. *Commun. Phys.* **3**, 18 (2020).
38. Gu, J. *et al.* Enhanced nonlinear interaction of polaritons via excitonic Rydberg states in monolayer WSe<sub>2</sub>. *Nat. Commun.* **12**, 2269 (2021).
39. Bae, Y. J. *et al.* Exciton-coupled coherent magnons in a 2D semiconductor. *Nature* **609**, 282-286 (2022).
40. Liu, H. & Shen, K. Spin wave dynamics excited by a focused laser pulse in antiferromagnet CrSBr. *Phys. Rev. B* **110**, 024424 (2024).
41. Scheie, A. *et al.* Spin waves and magnetic exchange hamiltonian in CrSBr. *Adv. Sci.* **9**, e2202467 (2022).
42. Uykur, E. *et al.* Phonon and magnon dynamics across the antiferromagnetic transition in the two-dimensional layered van der Waals material CrSBr. *Phys. Rev. B* **111**, 174434 (2025).

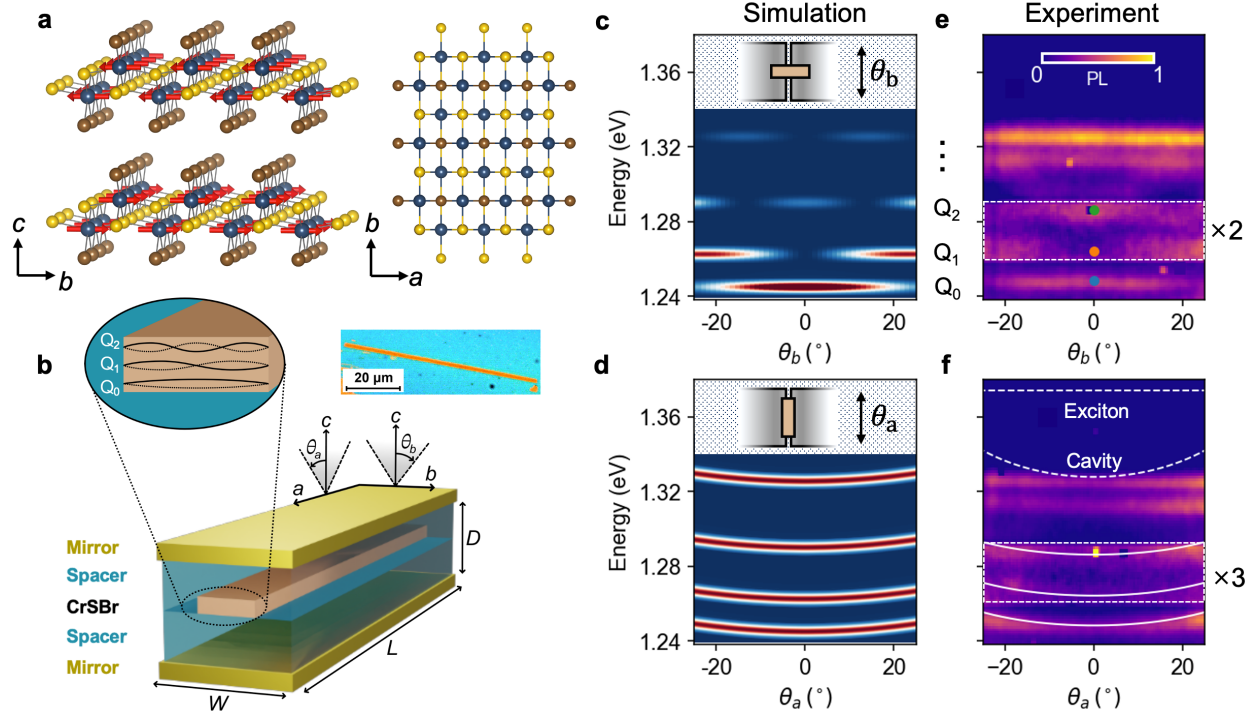


**Figure 1 | Exciton-polaritons in a CrSBr cavity wire.** **a**, Crystal structure of CrSBr viewed along the  $a$ - and  $c$ -axes (dark spheres, Cr; yellow spheres, S; brown spheres, Br). Red arrows indicate the magnetic order in the antiferromagnetic phase. **b**, Schematic of the CrSBr microcavity structure. The zoom-in indicates the spatial profile of the laterally quantized polariton modes. An exemplary micrograph of a CrSBr microcavity is shown at the top right corner. **c**, Simulated polariton dispersion along the short axis of the microwire obtained by modelling polaritons as particles in an elongated 2D rectangular potential well. Inset: In the experiment, we expect to resolve this dispersion when the  $b$ -axis of the microwire is aligned parallel to the entrance slit of the spectrometer. **d**, Simulated dispersion along the long axis of the microwire, equivalent to the experimental case where the  $a$ -axis of our microcavity is aligned parallel to the entrance slit of the spectrometer (inset). **e**, Angle-resolved normalized PL of cavity #1 dispersed along the  $b$ -axis, and **f**, along the  $a$ -axis measured using ultrafast photoexcitation ( $1.771$  eV;  $\Phi = 300 \mu\text{J}/\text{cm}^2$ ; pulse duration,  $140$  fs). PL signals in the white rectangular boxes are enhanced to increase visibility. The blue, orange and green dots in **e** indicate the ground state ( $Q_0$ ), and the first ( $Q_1$ ) and second ( $Q_2$ ) excited states obtained from a coupled oscillator model (see main text). The white dashed lines in **f** show the dispersions of uncoupled exciton and cavity photon modes. The solid white lines display the theoretically fitted lower polariton branches from the coupled oscillator model.

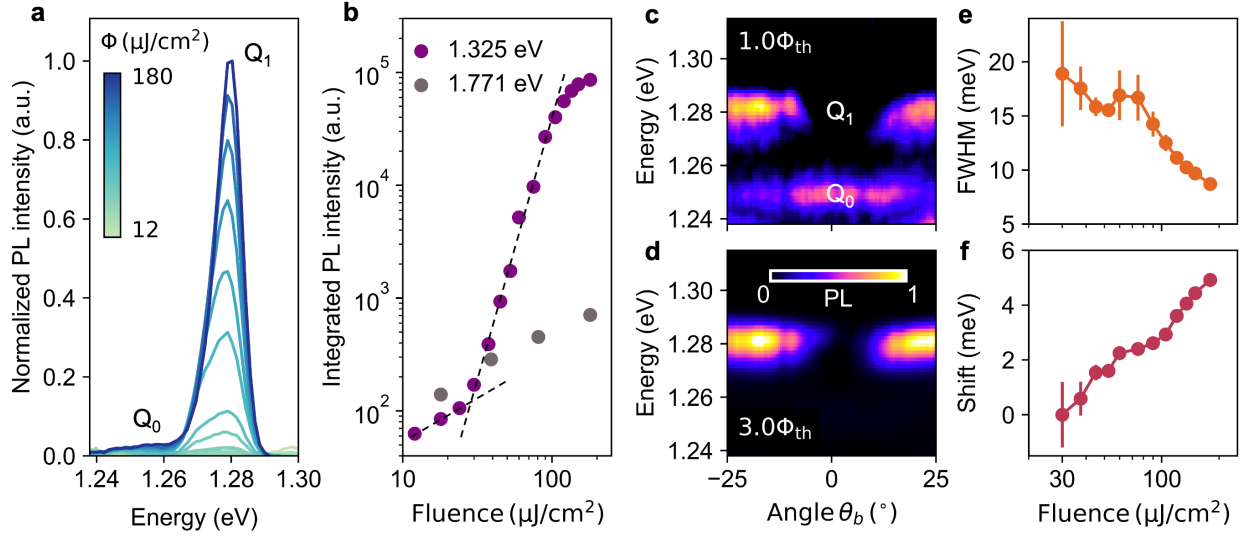


**Figure 2 | Nonlinear photoluminescence response and onset of exciton-polariton condensation.** **a**, Fluence-dependent normalized PL spectra of cavity #1 measured for a pump photon energy of 1.325 eV at 5 K. **b**, Fluence-dependent PL intensity for the peak at 1.276 eV (purple dots) in **a**. The grey dots represent the PL intensity at the same peak measured under off-resonant excitation using a photon energy of 1.771 eV. The black dashed lines serve as guides to the eye. **c-d**, Angle-resolved PL spectra at pump fluences of  $30 \mu\text{J}/\text{cm}^2$  and  $90 \mu\text{J}/\text{cm}^2$ . **e-f**, Linewidths and energy shifts of the PL peak at 1.276 eV in **a** as a function of pump fluence.

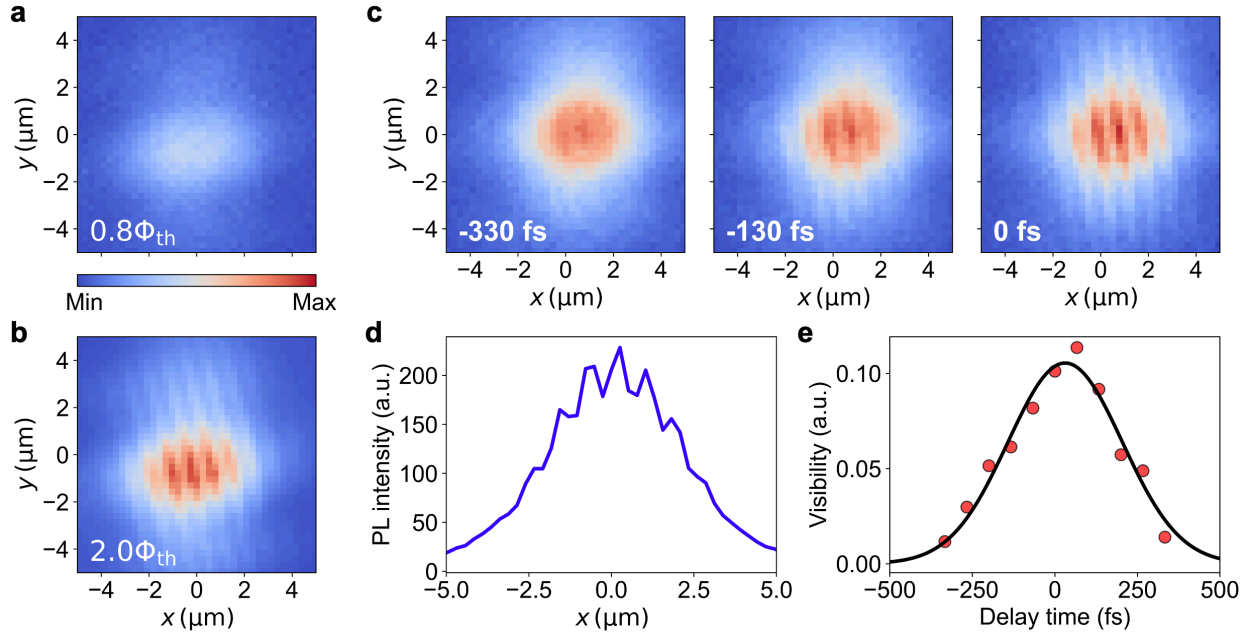


**Figure 3 | Spatial and temporal coherence of the exciton-polariton condensate.** Zero-delay spatial interference pattern of the exciton-polariton PL of cavity #1 at 5 K and a pump fluence of **a**,  $0.8\Phi_{th}$  and **b**,  $2.0\Phi_{th}$ , where  $\Phi_{th} = 30 \mu\text{J}/\text{cm}^2$ . **c**, Spatial interferogram of the exciton-polariton PL emission measured at delay times of  $t = -330$  fs,  $-130$  fs and  $0$  fs at a pump fluence of  $2.0\Phi_{th}$ . **d**, Interference fringes averaged along the direction perpendicular to the fringes for  $t = 0$  fs and a pump fluence of  $2.0\Phi_{th}$ . **e**, Visibility of the interference pattern in **d** as a function of delay time  $t$  at a pump fluence of  $2.0\Phi_{th}$ .

## Methods

**Optical spectroscopy and microscopy characterizations.** For the optical measurement, the microcavities are pumped by ultrafast laser pulses (repetition rate: 85 kHz, pulse duration: 140 fs) from an optical parametric amplifier (ORPHEUS; Light Conversion) driven by a commercial regenerative Yb:KGW laser amplifier system (PHAROS 10; Light Conversion). For optical imaging of the sample, we utilize a tungsten-halogen light source. To detect the photoluminescence, we use a spectrometer (Acton SP2500) coupled with a Peltier-cooled silicon charge-coupled device (CCD) camera (PIXIS 256) with a resolution of 1024×256 pixels. The sample is mounted in a closed-cycle cryostat and cooled down by liquid helium to 5 K.

Our optical setup allows us to access both the real-space and momentum-space images of the PL from the sample. To obtain the spectrum and real-space image, the emission from the sample is projected onto the imaging plane, i.e., the entrance slit of the spectrometer. To resolve the momentum (angle) distribution of the emission, an additional lens is placed into the beam path, such that the Fourier plane of the objective lens is projected on the entrance slit of the spectrometer.

The coherence measurements are conducted in a Michelson interferometer, with a retroreflector mounted in one of the two interferometric arms to invert vertically and horizontally the spatial coordinates of the real-space image. The relative temporal delay between the two arms is controlled by an optical delay line. The two interference images are overlapped by a lens on the slit of the spectrometer and imaged by the CCD camera.

**Coupled oscillator model.** The exciton-polariton dispersion is fitted by the coupled oscillator model<sup>1</sup>:

$$\begin{pmatrix} E_{\text{cav}} & \hbar\Omega/2 \\ \hbar\Omega/2 & E_{\text{exc}} \end{pmatrix} \begin{pmatrix} \alpha \\ \beta \end{pmatrix} = E \begin{pmatrix} \alpha \\ \beta \end{pmatrix}$$

Here  $E_{\text{cav}}$  and  $E_{\text{exc}}$  are the energies of the cavity photon and exciton, respectively.  $\hbar\Omega$  is the vacuum Rabi splitting, related to the exciton-photon coupling strength  $g$  following  $\hbar\Omega = 2g$ . Moreover,  $\alpha$  and  $\beta$  are the

amplitudes of the eigenvectors. The eigenvalues of the energy can be obtained by diagonalizing the matrix:

$$E_{\pm}(k) = \frac{E_{\text{cav}} + E_{\text{exc}}}{2} \pm \frac{1}{2} \sqrt{[E_{\text{cav}} - E_{\text{exc}}]^2 + \hbar^2 \Omega^2}$$

with  $E_+$  and  $E_-$  being upper and lower polariton branches.

Due to both the vertical and lateral quantum confinement of the cavity, the cavity photon mode can be further expressed as<sup>27-28</sup>:

$$E_{\text{cav}}(j, k_x) = \frac{\hbar c k_z}{n_c} \sqrt{1 + \left[ \frac{(j+1)\pi}{L_y} \right]^2 \frac{1}{k_z^2} + \left( \frac{k_x}{k_z} \right)^2}$$

Here,  $k_z = \pi/L_z$ , is the wave vector along the vertical direction of the cavity with  $L_z$  being the effective length of the cavity.  $k_x$  and  $k_y$  are the lateral wave vectors along the extended direction ( $a$ -direction in our case), and along the confined direction ( $b$ -direction), respectively. For each quantized mode  $j(= 0,1,2 \dots)$  along  $b$  direction,  $k_y = \pi(j+1)/L_y$  with  $L_y$  being the width of the cavity.

**'Particle in a box' simulation.** To obtain the dispersions shown in Fig. 1c,d, we solve the two-dimensional Schrödinger equation using the finite difference method implemented in an open-source code available under [https://github.com/LaurentNevou/Q\\_Schrodinger2D\\_demo](https://github.com/LaurentNevou/Q_Schrodinger2D_demo). The CrSBr flake is modelled as a rectangular potential well, whose dimensions are chosen according to the size of the sample. The barrier is set to 10 eV to mimic an infinite potential well. Consequently, the effective mass is the only free parameter of the model. The best agreement with the experimental data is obtained for effective masses  $m_a = m_b = 4.8 \times 10^{-5} m_0$  along the  $a$ -axis ( $m_a$ ) and  $b$ -axis ( $m_b$ ) with the free-electron mass  $m_0$ . For each eigenenergy, the obtained wavefunctions are converted to momentum-space using a fast Fourier transform (FFT). Finally, a Gaussian broadening in energy is applied for better comparability with the experiment.

### **Data availability**

The data sets generated during and/or analysed during the current study are available from the corresponding author upon reasonable request.

### **Acknowledgements**

The work at the University of Regensburg was supported by the Deutsche Forschungsgemeinschaft (DFG, German Research Foundation) through research grants HU1598/8 and SFB 1277, project-ID 314695032. N.N. acknowledges financial support by the Alexander von Humboldt Foundation. F.D. and J.H. acknowledge funding from the Emmy Noether Program (Project-ID 534078167). Z.S and K.M. were supported by project LUAUS25268 from Ministry of Education Youth and Sports (MEYS) and by the project Advanced Functional Nanorobots (reg. No. CZ.02.1.01/0.0/0.0/15\_003/0000444 financed by the EFRR). F.M. acknowledges funding from the Elite Network of Bavaria (ENB) and funding by the Bavarian State Ministry of Science and the Arts (StMWK).

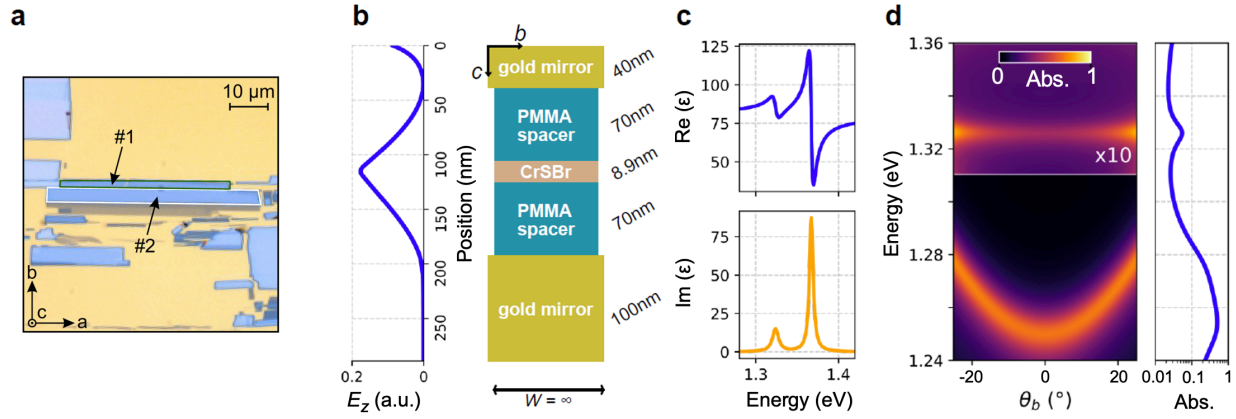
### **Author contributions**

F.D. and R.H. conceived the study. H.Z., N.N. and C.W. carried out the experiments. H.Z., N.N., J.H. and F.D. carried out the numerical calculations. I.G. prepared the cavity samples. K.M. and Z.S. grew the CrSBr flakes. F.M. carried out the quantization simulations. H.Z., J.H. and F.D. prepared the figures. All authors analysed the data, discussed the results and contributed to the writing of the manuscript.

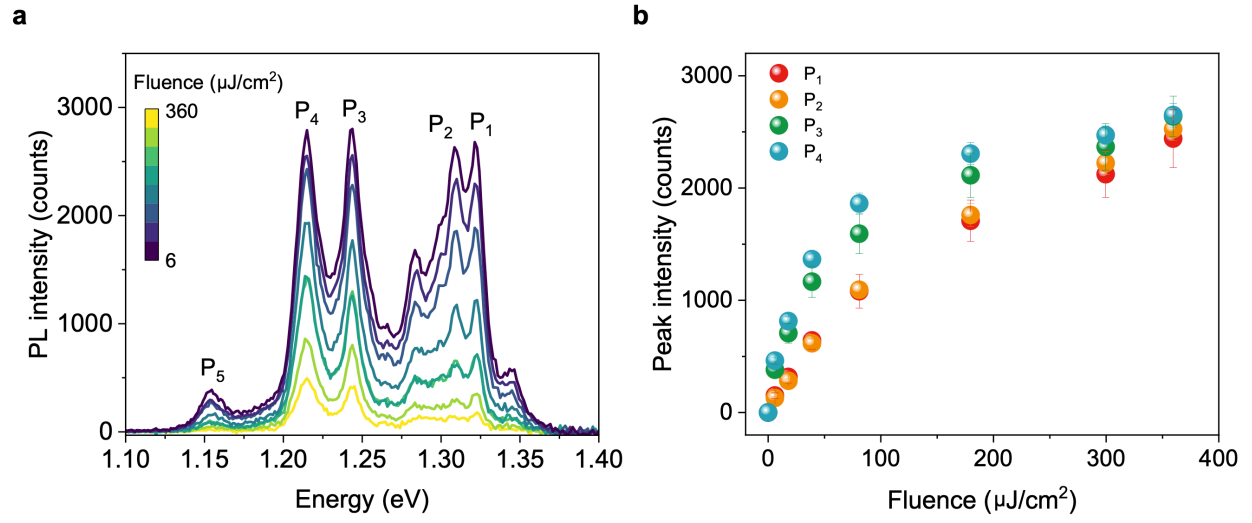
### **Competing interests**

The authors declare no competing interests.

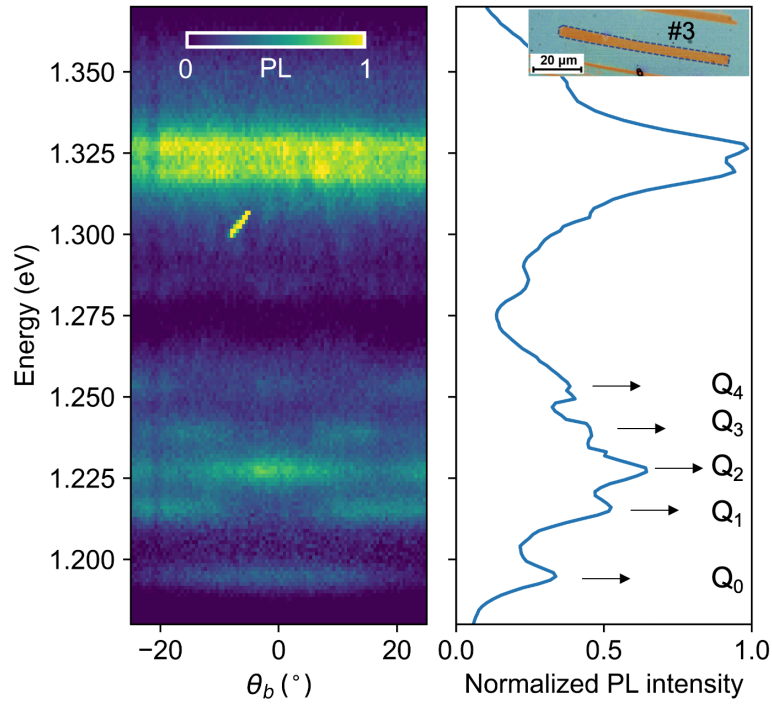
**Correspondence and requests for materials** should be addressed to F. Dirnberger.



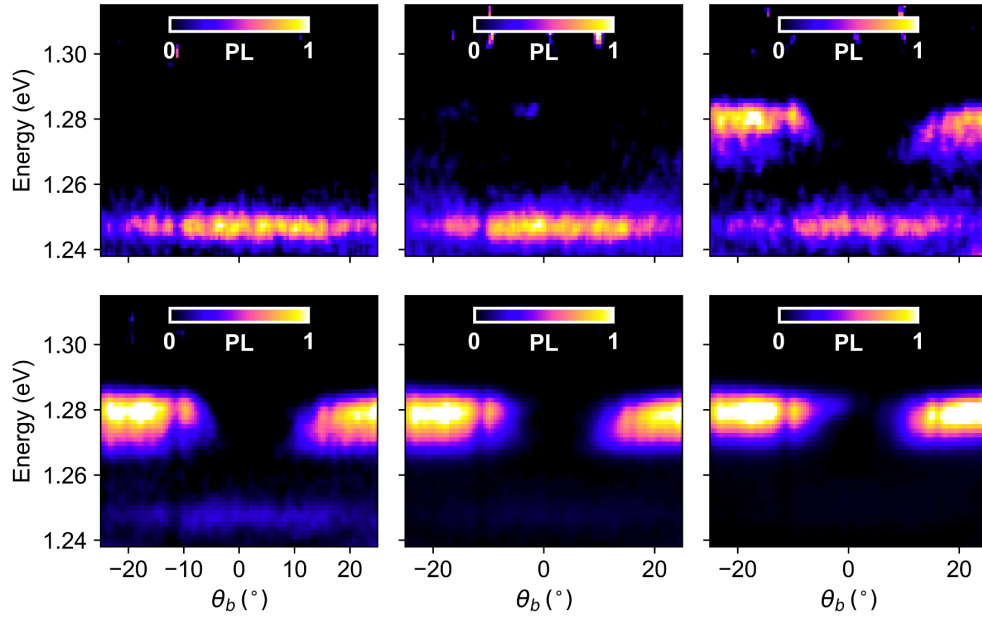
**Extended Data Fig. 1 | Characterization of cavity #1 and cavity #2.** **a**, Optical micrograph of cavity #1 and #2. **b**, Schematic of the CrSBr cavity and the electric field distribution along the c-direction. **c**, Real and imaginary parts of the CrSBr dielectric function used for numerical calculations. A Lorentz oscillator model accounts for contributions from bulk excitons, at 1.36 eV, and from surface excitons, at 1.33 eV (ref. <sup>23</sup>). **d**, Numerically calculated absorption of cavity #1 assuming infinite lateral extensions of the flake.



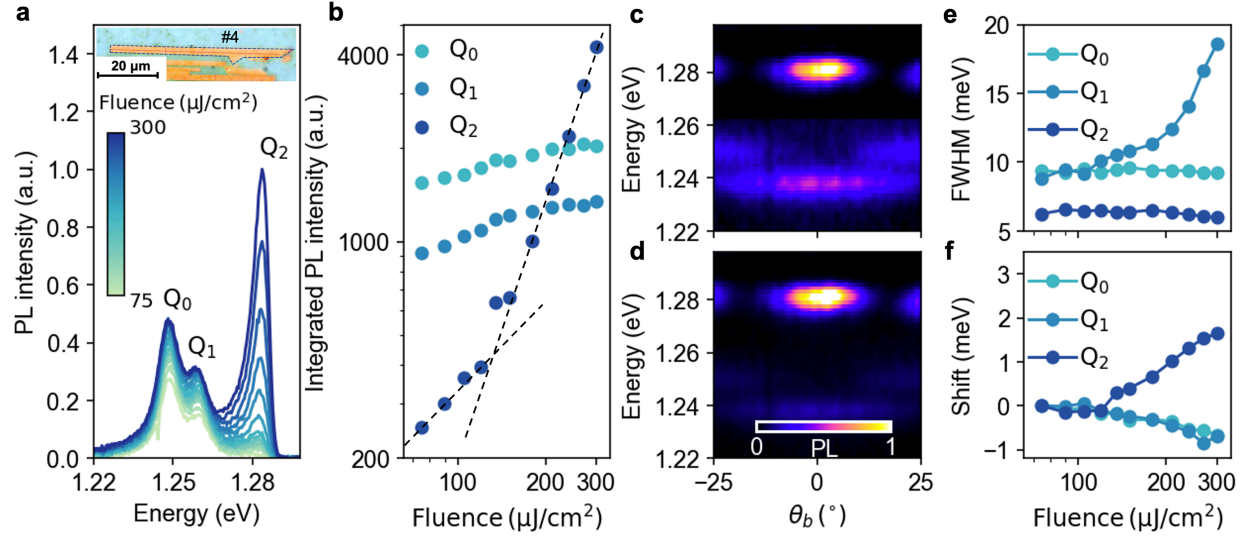
**Extended Data Fig. 2 | PL spectra of cavity #1 pumped by 1.771 eV laser excitation at 5 K. a,** Fluence dependent PL spectrum.  $P_3$  corresponds to  $Q_0$  of cavity #1 in the main text, while  $P_4$  and  $P_5$  are the residual signals from cavity #2. **b,** PL intensity for spectrum peaks  $P_1$ - $P_4$  labelled in **a** as a function of pump fluence.



**Extended Data Fig. 3 | Photoluminescence of cavity #3.** Left: Angle-resolved normalized PL along the  $b$ -axis, pumped by 1.771 eV laser excitation with a pump fluence of  $300 \mu\text{J}/\text{cm}^2$ . Right: Normalized PL spectrum. Inset: Optical micrograph of cavity #3. In the energy range between 1.19 eV and 1.26 eV, quantized states of  $Q_0$ - $Q_4$  are well resolved.



**Extended Data Fig. 4** | Fluence dependent Angle-resolved PL image for cavity #1 at 5 K, pumped by laser excitation at a photon energy of 1.325 eV and pump fluences of 15  $\mu\text{J}/\text{cm}^2$ , 30  $\mu\text{J}/\text{cm}^2$ , 45  $\mu\text{J}/\text{cm}^2$ , 60  $\mu\text{J}/\text{cm}^2$ , 90  $\mu\text{J}/\text{cm}^2$  and 150  $\mu\text{J}/\text{cm}^2$  (upper left to lower right panels).



**Extended Data Fig. 5 | Nonlinear photoluminescence response and onset of exciton-polariton condensation for cavity #4 pumped by 1.325 eV laser excitation at 5 K.** **a**, Pump fluence dependent normalized PL spectra. Inset: Optical micrograph of cavity #4. **b**, Pump fluence dependent PL intensity of the peaks  $Q_0$ ,  $Q_1$ ,  $Q_2$ , as labelled in **a**. **c-d**, Angle-resolved, PL spectra normalized to the maximum intensity at energies of 1.28 eV, for pump fluences of  $150 \mu\text{J}/\text{cm}^2$  and  $300 \mu\text{J}/\text{cm}^2$  respectively. **e-f**, Linewidths and energy shifts of the PL peaks  $Q_0$ ,  $Q_1$ ,  $Q_2$  as a function of pump fluence.